Prospects for cosmic magnification measurements using HI intensity mapping

Amadeus Witzemann[1*], Alkistis Pourtsidou[2,1], Mario G. Santos[1,3]
[1] *Department of Physics & Astronomy, University of the Western Cape, Cape Town 7535, South Africa*
[2] *School of Physics and Astronomy, Queen Mary University of London, Mile End Road, London E1 4NS, UK*
[3] *South African Radio Astronomy Observatory (SARAO), 2 Fir Street, Observatory, Cape Town, 7925, South Africa*

ABSTRACT
We investigate the prospects of measuring the cosmic magnification effect by cross-correlating neutral hydrogen intensity mapping (HI IM) maps with background optical galaxies. We forecast the signal-to-noise ratio for HI IM data from SKA1-MID and HIRAX, combined with LSST photometric galaxy samples. We find that, thanks to their different resolutions, SKA1-MID and HIRAX are highly complementary in such an analysis. We predict that SKA1-MID can achieve a detection with a signal-to-noise ratio of ~ 10 on a multipole range of $\ell \lesssim 200$, while HIRAX can reach a signal-to-noise ratio of ~ 30 on $200 < \ell < 2000$. We conclude that measurements of the cosmic magnification signal will be possible on a wide redshift range with foreground HI intensity maps up to $z \lesssim 2$, while optimal results are obtained when $0.6 \lesssim z \lesssim 1.3$.

Key words: cosmology: large-scale structure of the universe – gravitational lensing: weak

1 INTRODUCTION

Traveling through the Universe, the path of light is deflected by the mass distribution it encounters. Images of distant light sources are distorted by the intervening matter along the line of sight (LOS), an effect well described by General Relativity. As a result, distortions of shapes, magnifications and even duplicate images are observed and are generally classified as weak or strong gravitational lensing.

Weak gravitational lensing or cosmic shear is a coherent distortion of the shapes of galaxies, and has been routinely detected using optical galaxy surveys, with the first detections reported almost two decades ago (see, for example, Bacon et al. (2000); Kaiser et al. (2000); van Waerbeke et al. (2000); Wittman et al. (2000)). Ongoing and forthcoming large scale structure surveys like CFHTLens (Heymans et al. 2012), DES (Abbott et al. 2016), Euclid (Amendola et al. 2018), and LSST (Abate et al. 2012), will give precise cosmic shear measurements and use them to constrain the properties of dark energy. The accuracy and robustness of weak lensing measurements depends on the control of various systematic effects such as intrinsic alignments, point spread function, seeing and extinction, as well as photometric redshift calibration (Mandelbaum 2018). In addition, Stage IV lensing surveys with Euclid and LSST will need accurate theoretical modelling of nonlinear clustering and baryonic

effects down to very small scales to achieve their goals. Further improvements will come from the use of galaxy-galaxy lensing cross-correlations (van Uitert et al. 2018).

In addition to the distortion of galaxy shapes, there is another form of lensing, cosmic magnification, which can be measured even when the sizes and shapes of sources are inaccessible. This makes it particularly attractive as it is free from many systematics such as the point spread function and intrinsic alignments (see, for example, Zhang & Pen (2006), which discussed the possibility of using radio galaxy surveys to detect this effect). Magnification occurs when intervening structure between an observer and a source acts to magnify or demagnify the object, i.e. sometimes allowing the observer to see objects otherwise too faint (Bartelmann & Schneider 2001). However, the apparent observed area can also be increased, which leads to an apparent decrease in number counts if the total number is conserved. Only slightly altering the observed structures, this effect is notoriously difficult to measure (see e.g. the discussion in Hildebrandt et al. (2009)). Several promising techniques exist, but there have been only a few, and controversial, detections (see discussion and references in Scranton et al. (2005)). The first time this signal was measured with high significance was the 8σ detection achieved in Scranton et al. (2005) using the Sloan Digital Sky Survey and the galaxy-quasar cross-correlation. A more recent analysis with DES galaxies is presented in Garcia-Fernandez et al. (2018).

Measurements of cosmic magnification probe the galaxy

halo occupation distribution, dark matter halo ellipticities and the extent of galaxy dust halos (Scranton et al. 2005; Menard et al. 2010) – they are complementary to shear-shear measurements, and they can be used to break parameter degeneracies (Van Waerbeke et al. 2010). Similar to cosmic shear, cosmic magnification provides constraints on the galaxy-matter correlation, but without the requirement of measuring shapes, it suffers from less systematic errors and can be extended to sources at much higher redshifts (Scranton et al. 2005). In addition to probing the matter distribution directly, magnification also plays an important role in *geometrical methods* to measure dark energy parameters independently of the matter power spectrum (Jain & Taylor 2003; Bernstein & Jain 2004; Taylor et al. 2007). These methods use galaxy-lensing correlations and therefore depend on estimates of the galaxy density. This is directly affected by magnification, which can therefore introduce systematic errors unless corrected for (Scranton et al. 2005; Hui et al. 2007; Ziour & Hui 2008; Bonvin & Durrer 2011).

A straightforward approach to measure magnification uses the angular cross-correlation between foreground and background galaxy counts (see e.g. Hildebrandt et al. 2009), where galaxy-magnification or magnification-magnification cross-correlations would be major contributors to a non-zero signal.

Following a similar line of thought, we propose to use HI intensity maps acting as foreground lenses, magnifying a background distribution of galaxies. A motivation for using HI is that intensity maps have no lensing corrections at first order due to flux conservation (Hall et al. 2013), which removes magnification-magnification correlations between foreground and background. This potentially decreases the signal, but also helps interpretation by removing additional terms in the signal calculation. In addition, the excellent redshift resolution of the foreground HI maps allows to combine measurements using different slices of the HI distribution. Using HI intensity maps also mitigates the danger of overlapping foreground and background sources, which results to a clustering (not lensing) signal. Furthermore, radio and optical observations are subject to different systematic effects, which are expected to drop out in cross-correlation. In the following, we derive forecasts for a potential detection of the magnification signal, using noise properties for the planned radio telescopes SKA1-MID (Bacon et al. 2018) and HIRAX (Newburgh et al. 2016), as well as LSST.

The plan of the paper is as follows: In section 2 we give an introduction to cosmic magnification statistics and introduce the possibility of using HI intensity maps as foreground lenses. In section 3 we calculate the instrumental (thermal) noise of SKA1-MID and HIRAX, as well as the shot noise from the LSST sample, and investigate the signal and noise properties for the cosmic magnification measurement. In section 4 we optimise the signal-to-noise ratio for our proposed method and derive the cumulative signal-to-noise ratio for SKA1-MID and HIRAX. We summarise our findings and conclude in section 5.

2 COSMIC MAGNIFICATION STATISTICS

In this section we describe the power spectrum formalism for measuring the cosmic magnification signal from background galaxies. We start with the standard approach, which assumes a galaxy sample as the foreground sample, and then introduce the possibility of using HI intensity maps instead.

2.1 Galaxies as the foreground sample

Galaxies are biased tracers of the underlying dark matter distribution, which is thought to contain most of the mass distributed along the LOS to a light source. Magnification will increase the flux from a galaxy, making it appear brighter than it actually is. Therefore galaxies normally too faint to be detected can still be seen if the magnification caused by the matter along the LOS is strong enough. However, the apparent area of a source is also increased, resulting in a decrease of the observed number density of galaxies. We can write (Zhang & Pen 2006)

$$\delta_{\rm g}^{\rm L} = \delta_{\rm g} + (5s_{\rm g} - 2)\kappa + \mathcal{O}(\kappa^2) \,, \tag{1}$$

with $\delta_{\rm g}^{\rm L}$ and $\delta_{\rm g}$ the lensed and unlensed intrinsic galaxy overdensities, respectively, and κ the lensing convergence. For a survey with limiting magnitude $m^\star$ the number count slope $s_{\rm g}$ is given by (Duncan et al. 2014)

$$s_{\rm g} = \frac{d \log_{10} n_{\rm g}(< m^\star)}{dm^\star} \,, \tag{2}$$

with the cumulative number of detected galaxies per redshift interval and unit solid angle, $n_{\rm g}$. The cross-correlation of well separated foreground (at position $\theta_{\rm f}$ and redshift $z_{\rm f}$) and background ($\theta_{\rm b}$ and $z_{\rm b}$) galaxy samples is free from the intrinsic galaxy over-density correlation term $\langle \delta_{\rm g}(\theta_{\rm f}, z_{\rm f}) \delta_{\rm g}(\theta_{\rm b}, z_{\rm b}) \rangle$, therefore

$$\begin{aligned} \langle \delta_{\rm g}^{\rm L}(\theta_{\rm f}, z_{\rm f}) \delta_{\rm g}^{\rm L}(\theta_{\rm b}, z_{\rm b}) \rangle &= \langle (5s_{\rm g}^{\rm b} - 2)\kappa_{\rm b} \delta_{\rm g}(\theta_{\rm f}, z_{\rm f}) \rangle \\ &+ \langle (5s_{\rm g}^{\rm f} - 2)(5s_{\rm g}^{\rm b} - 2)\kappa_{\rm f}\kappa_{\rm b} \rangle \,, \end{aligned} \tag{3}$$

where the superscript L denotes lensed quantities. The right hand side of equation 3 contains the magnification-galaxy ($\mu - {\rm g}$) correlation (first term) and the magnification-magnification ($\mu - \mu$) correlation (second term). The latter is subdominant for foregrounds at comparably low redshifts and therefore usually neglected. If both foreground and background galaxies are at high redshifts, however, it can become large (Ziour & Hui 2008).

2.2 HI intensity maps as the foreground sample

In this work, we focus on the magnification effect of HI intensity maps in the foreground, acting on the clustering statistics of background galaxies. Intensity maps themselves are not lensed at linear order due to surface brightness conservation (Hall et al. 2013). This means that $s_{\rm HI} = 2/5$ and

$$\delta T_{21}^{\rm L} = \delta T_{21} = \bar{T}_{21} \delta_{\rm HI} = \bar{T}_{21} b_{\rm HI} \delta \,, \tag{4}$$

where $\bar{T}_{21}$ is the mean brightness temperature of neutral hydrogen, $b_{\rm HI}$ is the hydrogen bias and δ the dark matter over-density. Considering galaxies as the background sample, we now have

$$\langle \delta_{\rm HI}^{\rm L}(\theta_{\rm f}, z_{\rm f}) \delta_{\rm g}^{\rm L}(\theta_{\rm b}, z_{\rm b}) \rangle = \langle (5s_{\rm g}^{\rm b} - 2)\kappa_{\rm b} b_{\rm HI} \delta(\theta_{\rm f}, z_{\rm f}) \rangle \,, \tag{5}$$

where the magnification-magnification term is absent since $s_{\rm HI} = 2/5$. The above relation holds at all redshifts, given
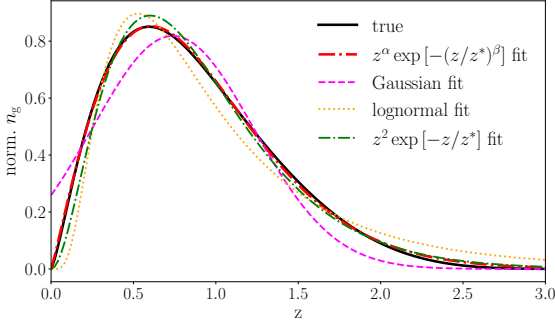
Figure 1. Different fitting functions for the cumulative galaxy number count were considered. The normalised 'true' function here is taken from Alonso et al. (2015) (solid black line). The best fitting function (red dotted-dashed line) is given in Equation (11).

that the foreground and background samples are well separated. This can be guaranteed via the excellent redshift information provided by the intensity mapping survey.

The observable magnification signal can be expressed using the angular power spectrum (Zhang & Pen 2006; Ziour & Hui 2008)

$$C_\ell^{\mathrm{HI}-\mu}(z_\mathrm{f}, z_\mathrm{b}) = \frac{3}{2} \frac{H_0^2}{c^2} \Omega_{\mathrm{m},0} \times$$
$$\int_0^\infty dz \frac{b_{\mathrm{HI}} \bar{T}_{21}(z) W(z, z_\mathrm{f}) g(z, z_\mathrm{b})}{r^2(z)} (1 + z) \times$$
$$P_\mathrm{m}((\ell + 1/2)/r(z), z), \qquad (6)$$

where $r(z)$ is the comoving distance to redshift z and we have applied the Limber approximation, valid for $\ell \geqslant 10$ (Limber 1954; Loverde & Afshordi 2008). The redshift distribution of the foreground HI intensity maps is given by a top hat over the foreground redshift bin $W(z, z_\mathrm{f})$ and $g(z, z_\mathrm{b})$ is the lensing kernel:

$$g(z, z_\mathrm{b}) = \frac{r(z)}{N_\mathrm{g}(z_\mathrm{b})} \int_{z_\mathrm{b}^{\min}}^{z_\mathrm{b}^{\max}} dz' \frac{r(z') - r(z)}{r(z')} (5s_\mathrm{g}(z') - 2) n_\mathrm{g}(z'), \qquad (7)$$

where the number of galaxies per square degree in the background bin is

$$N_\mathrm{g}(z_\mathrm{b}) \equiv \int_{z_\mathrm{b}^{\min}}^{z_\mathrm{b}^{\max}} n_\mathrm{g}(z) dz, \qquad (8)$$

and $z_\mathrm{b}^{\min}$, $z_\mathrm{b}^{\max}$ denote the minimum and maximum redshift for the background galaxy sample. An interesting feature of the geometrical weight $\frac{r(z') - r(z)}{r(z')}$ is that, in a flat universe, it takes the form of a parabola with a maximum at $r(z') = r/2$. Thus, structures half-way between the source and the observer are the most efficient to generate lensing distortions (Kilbinger 2015) (and very low redshift foregrounds are less favoured).

For increased computational speed, we use a fitting function to approximate the cumulative galaxy count for LSST, n_g, provided in the publicly available code from Alonso et al. (2015). This code in turn uses the Schechter function (Schechter 1976) for the r'-band luminosity from

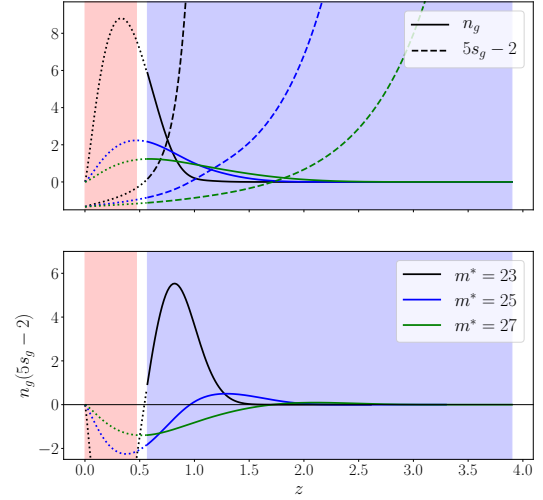**Figure 2.** We illustrate the behavior of the number count slope s_g and galaxy count n_g with respect to the magnitude threshold m^*, here with foreground redshift $0 < z < 0.47$, which corresponds to band 2 of SKA1-MID, described in detail in section 3. The red (blue) shaded areas indicate the foreground (background) redshift range. The upper panel displays the galaxy number density n_g (normalised to integrate to one inside the background bin), and the contribution of the number count slope s_g. The bottom panel shows the product $n_\mathrm{g}(5s_\mathrm{g} - 2)$, which is the only term inside the integral Equation (7) to potentially be negative. This demagnification leads to cancellation in the integration and thus to a smaller lensing signal. An appropriate magnitude cutoff enforces $5s_\mathrm{g} > 2$ in the background redshift bin and thus boosts the signal. However, this comes at the cost of increasing the galaxy shot noise.
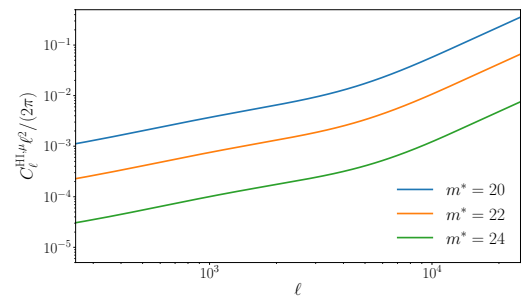

Figure 3. The HI-magnification cross-correlation power spectrum for a foreground redshift from $z = 0$ to 0.47, corresponding to band 2 of SKA1-MID. Lower magnitude cuts increase the magnification signal.

Gabasch et al. (2006), with the faint end slope $\alpha = -1.33$, the characteristic magnitude M^*

$$M_*(z) = M_0 + a \ln(1 + z) \qquad (9)$$

and the density ϕ^*

$$\phi_*(z) = (\phi_0 + \phi_1 z + \phi_2 z^2)[10^{-3} \mathrm{Mpc}^{-3}]. \qquad (10)$$

Here $M_0 = -21.49$, $a = -1.25$, $\phi_0 = 2.59$, $\phi_1 = -0.136$, $\phi_2 = -0.081$. We adapt the fit from LSST Science Collaboration et al. (2009) to approximate n_g as follows,

$$n_g(z) \propto z^\alpha \exp\left(-\left(\frac{z}{z^*}\right)^\beta\right), \tag{11}$$

where we optimise the parameters α, β and z^* to fit n_g from Alonso et al. (2015) as functions of magnitude cutoff m^* by interpolation. Fig. 1 compares this fit with the true n_g and with several other fitting functions. The overall amplitude is irrelevant in Equation (7), as n_g is normalised to integrate to one, but it is required to calculate the shot noise – see section 3 for details.

The number count slope s_g (Fig. 2) rises quicker for a lower magnitude cutoff, therefore the magnitude threshold can be chosen to avoid a sign change of $5s_g - 2$ in the background redshift bin. The amplitude of the magnification signal is proportional to a redshift integral of $5s_g - 2$ (Equations (2) and (6)). An appropriate magnitude cutoff thus boosts the signal by avoiding cancellations inside the integral for the lensing kernel g. Fig. 2 demonstrates this in a situation where a lower magnitude threshold is beneficial to optimise the magnification signal, which is shown in Fig. 3. Decreasing m^* comes at the cost of a smaller number of observed galaxies and therefore increased shot noise. We optimise to achieve a maximal signal to noise ratio. We will further discuss this in section 3.2, and we also note that a number count slope weighting was suggested in (Menard & Bartelmann 2002) and used in the SDSS data analysis of Scranton et al. (2005).

We use `CAMB` with `HALOFIT` (Lewis et al. 2000; Smith et al. 2003; Takahashi et al. 2012) to estimate the nonlinear matter power spectrum, $P_m(k, z)$, assuming a flat ΛCDM cosmology with $h = 0.678$, $\Omega_c h^2 = 0.119$, $\Omega_b h^2 = 0.022$, $n_s = 0.968$.

The error in the measurement of the cross-correlation power spectrum is

$$\Delta C_\ell^{HI-\mu} = \sqrt{\frac{2((C_\ell^{HI-\mu})^2 + (C_\ell^{gg} + C^{shot})(C_\ell^{HI-HI} + N_\ell))}{(2\ell + 1)\Delta\ell f_{sky}}}, \tag{12}$$

where C^{shot} is the galaxy shot noise power spectrum, N_ℓ is the thermal noise of the intensity mapping instrument, $\Delta\ell$ is the binning in multipole space, and f_{sky} is the fraction of sky area overlap of the HI and optical surveys. For the foreground HI IM sample we use a top-hat window function $W(z) = 1/\Delta z$ inside the bin of width Δz and zero elsewhere. We can then write the HI and galaxies autocorrelation power spectra as

$$C_\ell^{HI-HI} = \frac{H_0}{c} \int dz E(z) \left(\frac{b_{HI}\bar{T}_{21}(z)W(z)}{r}\right)^2 P_m\left(\frac{\ell + 1/2}{r}, z\right), \tag{13}$$

and

$$C_\ell^{g-g} = \frac{H_0}{cN_g^2} \int dz E(z) \left(\frac{b_g(z)n_g(z)}{r}\right)^2 P_m\left(\frac{\ell + 1/2}{r}, z\right), \tag{14}$$

where we have written the Hubble rate as $H(z) = H_0 E(z)$, and the HI bias b_{HI} is given by fits to the results from Alonso et al. (2015):

$$b_{HI}(z) = 0.67 + 0.18z + 0.05z^2. \tag{15}$$

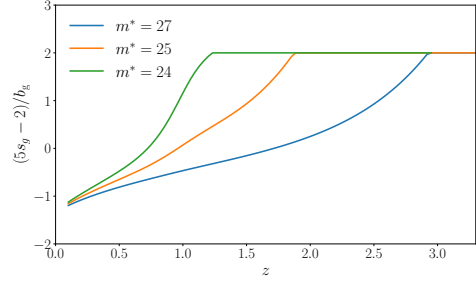The galaxy bias b_g naturally depends on redshift as well

Figure 4. The ratio of number count slope and galaxy bias $(5s_g - 2)/b_g$ for different magnitude cutoff values. The ratio is set to 2 for higher redshifts via the choice of galaxy bias, see Equation (17). The maximum magnitude detectable with LSST is assumed to be 27. Imposing a lower magnitude cutoff increases the shot noise, but also the number count slope, which increases the magnification signal.

as magnitude cutoff, as brighter objects are rarer and thus more biased, an effect which is ignored when a simple linear and dererministic fitting function is used, for example

$$\tilde{b}_g(z) = 1 + 0.84z. \tag{16}$$

To enforce a behaviour similar to that of the magnification bias at higher redshifts and more stringent magnitude cuts, we use a piecewise differentiable galaxy bias:

$$b_g(z) = \max\left(\tilde{b}_g, \frac{1}{2}(5s_g - 2)\right). \tag{17}$$

This choice makes sure that the ratio $(5s_g - 2)/b_g$ converges, as described in (Hui et al. 2007), and the resulting ratio is shown in Fig. 4 for different magnitude cutoff values. We note that this choice has a comparably weak effect on our results, as the signal remains unaltered and, as it will be shown, errors are mostly shot noise dominated.

The mean observed HI brightness temperature is calculated using the fit provided in Santos et al. (2017), which is based on the results from Santos et al. (2015):

$$\bar{T}_{21} = 0.0559 + 0.2324z - 0.024z^2 \text{ mK}. \tag{18}$$

3 ERROR CALCULATIONS

3.1 HI intensity maps

We consider the experiments HIRAX and SKA1-MID to map the distribution of HI, used as the foreground sample. Together with the shot noise from LSST, their instrumental noise contributes to the total error budget given by Equation (12).

HIRAX is a planned radio interferometer of 6 m diameter dishes, sharing the site in the Karoo in South Africa with MeerKAT and SKA1-MID. We assume the full planned array of 1024 and the reduced set of 512 dishes, arranged in a dense square grid with 1 m space between individual antennas. HIRAX aims to perform a large sky intensity mapping survey with $15,000$ deg^2 area, and the integration time is taken to be two full years (corresponding to 4 years observation). We assume a constant system temperature of 50 K on its entire frequency coverage ranging from 400 to 800 MHz (Newburgh et al. 2016).

At the same time, SKA1 is assumed to have only one year worth of integration time but a larger survey area of 16,900 deg^2. This corresponds to the maximum possible survey overlap with LSST, after taking into account the total survey area of SKA1-MID (Santos et al. 2015) and contamination from galactic synchrotron radiation and dust. SKA1-MID will consist of different dish types: the (already operating) 64 MeerKAT dishes with 13.5 m, and 133 SKA1-MID dishes of 15 m diameter. For simplicity, we assume all dishes to be identical, taking an average dish diameter $\tilde{D}_{\rm dish} = (64 \times 13.5 + 133 \times 15)/(64+133)$ m and using a Gaussian beam pattern. We consider two observational bands: band 1 ranging from 350 to 1050 MHz, and band 2 from 950 to 1750 MHz (Bacon et al. 2018). The system temperature is assumed to be 30 K for band 1 and 20 K for band 2. This is conservative on low redshifts. For high-redshift foreground bins, the system temperature increases beyond that, but at the same time the galaxy shot noise becomes the dominant source of error and magnification detections quickly become extremely difficult for foreground samples with $z \gtrsim 2$. This justifies our assumption of constant system temperature for both SKA1-MID and HIRAX. For both experiments, we use equally spaced redshift bins of width $\Delta z = 0.5$, with the exception of band 2 with $\Delta z = 0.47$. A more realistic treatment would have to take into account the frequency dependence of the noise temperatures of both experiments, and the different dish and receiver types of SKA1. However, we expect this to have a negligible effect on our results.

Following Battye et al. (2013) and Bull et al. (2015) for the intensity mapping noise calculations, we calculate the single dish noise for SKA1-MID as

$$N_\ell^{\rm SD} = \sigma_{\rm pix}^2 \Omega_{\rm pix} W_\ell^{-1}. \tag{19}$$

Here, we use the solid angle per pixel $\Omega_{\rm pix} = 4\pi f_{\rm sky}/N_{\rm pix}$, the number of pixels $N_{\rm pix}$, the beam ($\Theta_{\rm FWHM}$) smoothing function $W_\ell = \exp\left(-\ell^2 \Theta_{\rm FWHM}^2/(8\ln 2)\right)$, the pixel noise $\sigma_{\rm pix} = T_{\rm sys}\sqrt{N_{\rm pix}/(t_{\rm tot}\delta_\nu N_{\rm dish})}$ and the frequency resolution (channel width) δ_ν.

For HIRAX, we calculate the interferometer noise

$$N_\ell^{\rm INT} = \frac{(\lambda^2 T_{\rm sys})^2}{2A_{\rm e}^2 d\nu n(u) t_{\rm p}}, \tag{20}$$

with the frequency bin width $d\nu$, the time per pointing $t_{\rm p} = t_{\rm tot}/N_{\rm p}$, the effective collecting area of one dish $A_{\rm e} = (D_{\rm dish}/2)^2\pi$, and using the relation $u = \ell/(2\pi)$ for the baseline density $n(u)$.

For all experiments we assume full survey overlap with LSST.

3.2 Photometric galaxy counts

We normalise the LSST sample to be a total of $\sim 6.3 \times 10^9$ galaxies at $m^* = 27$[1]. The galaxy shot noise for LSST is calculated as $C^{\rm shot} = 4\pi/N_{\rm g}^{\rm LSST}(z)$, where we use a fitting function to calculate the number of detected galaxies in the considered redshift bin, $N_{\rm g}^{\rm LSST}$ (Eqs. (8) and (11)). We consider all possible LSST redshift bins to have their upper edge

at the same $z_{\rm max}^{\rm LSST} = 3.9$, and the lower bin edge at a separation from the upper edge of the foreground bin, $z_i^{\rm fg} + 0.1$. The choice of a separation of $\Delta z = 0.1$ is conservative, ruling out any cross-correlations from possible overlaps, caused for example by the uncertainty in the photometric redshift measurements of LSST. We calculate the number count slope for LSST using an adjusted version of the code provided in Alonso et al. (2015) to extend to more stringent luminosity cutoffs m^*. We then interpolate $(5s_{\rm g} - 2)n_{\rm g}$ on a fine grid (z and m^*) to speed up the numerical calculations.

In order to illustrate the different error contributions and consolidate our findings, Fig. 5 shows all summands contributing to the HI-magnification cross correlation error:

$$(\Delta C_\ell^{\rm HI-\mu})^2 = \frac{2}{(2\ell+1)\Delta\ell f_{\rm sky}}\left((C_\ell^{\rm HI-\mu})^2 + C_\ell^{\rm g-g}C_\ell^{\rm HI-HI}\right.$$
$$\left. + C^{\rm shot}C_\ell^{\rm HI-HI} + N_\ell C_\ell^{\rm g-g} + C^{\rm shot}N_\ell\right). \tag{21}$$

The amplitude of the different contributions here depends on the choice of experiments and redshift binning.

To ease comparison we used the same single redshift bin for HIRAX and SKA1-MID in Fig. 5, from $z = 0.85$ to 1.35. For HIRAX a magnitude cutoff of $m^* = 24.4$ maximises the signal-to-noise ratio; for SKA1-MID it is 24.3. This optimisation will be discussed further in section 4. In this case shot noise dominates the error throughout, but it becomes comparable to cosmic variance (mostly $C_\ell^{\rm g-g}C_\ell^{\rm HI-HI}$) on large scales for SKA1-MID. Note that small scales are practically inaccessible for SKA1-MID due to its poor angular resolution, restricting it to much larger scales than HIRAX.

The multipole resolution is set by the maximum scale accessible by the SKA, i.e. the survey area $S_{\rm area}$ when in single dish mode. We estimate $\ell_{\rm min}^{\rm SKA} = 2\pi/\sqrt{S_{\rm area}} \sim 3$, but choose a more conservative value of $\ell_{\rm min}^{\rm SKA} = 10$ for the Limber approximation to hold (Loverde & Afshordi 2008). For the HIRAX interferometer it is set by the field of view (fov) which depends on frequency. For the sake of simplicity we ignore this dependence and assume a mean fov $= 35.5$ deg^2 (Newburgh et al. 2016), giving $\ell_{\rm min}^{\rm HIRAX} = 2\pi/\sqrt{\rm fov} \sim 60$. From the signal to noise ratio $C_\ell^{\rm HI-\mu}/\Delta C_\ell^{\rm HI-\mu}$ we calculate the cumulative (total) signal to noise as

$$\mathrm{SN}_{\rm tot} = \sqrt{\sum_{\bar\ell = \ell_{\rm min}}^{\ell}(C_{\bar\ell}^{\rm HI-\mu}/\Delta C_{\bar\ell}^{\rm HI-\mu})^2}, \tag{22}$$

where the sum runs over the relevant ℓ values, with the minimum ℓ, and the binning $\Delta\ell$, set by $\ell_{\rm min}$. We note, however, that the cumulative signal to noise ratio $\mathrm{SN}_{\rm tot}$ is binning independent.

4 RESULTS AND DISCUSSION

We maximise the signal to noise ratio with respect to the galaxy magnitude threshold m^* for each HI survey and redshift bin. We consider an optimisation range of $m^* \in [19, 27]$ and plot $\mathrm{SN}(m^*)_{\rm tot}$ for a few examples in Fig. 6. The optimal values we found (using the *python* package *scipy optimize*) are shown in Table 1. Generally, for low-redshift foreground bins, also a low m^* is preferred, which increases the number

---

[1] This is slightly more conservative than the number quoted in LSST Science Collaboration et al. (2009), i.e. almost 10^{10} galaxies for $m^* = 27.5$.
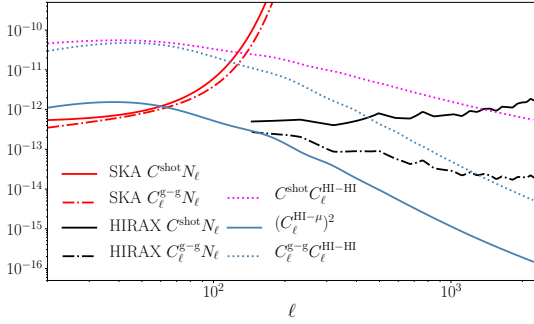
Figure 5. All contributions to $\Delta C_\ell^{\mathrm{HI}-\mu}$ as in Equation (21), for a foreground redshift bin from $z = 0.85$ to 1.35 and a background bin $z \geqslant 1.45$. The common factor of $2/((2\ell+1)\Delta\ell f_{\mathrm{sky}}$ was omitted here. Terms proportional to the SKA1-MID (HIRAX) noise are plotted in red (black) and terms proportional to shot noise and cosmic variance are plotted cyan and steel blue respectively. For this choice of binning, the HI intensity mapping noise is subdominant, followed by pure cosmic variance, but both dominated by terms with shot noise, the biggest source of error. Note that the choice of intermediate foreground and background redshift in this plot is only to ease comparison, but not necessarily ideal for magnification measurements.

	SKA1 B1	-	-	-
z range	0.34-0.84	0.84-1.34	1.34-1.84	1.84-2.34
m^*	23.6	23.1	26.3	27.0
$\mathrm{SN_{tot}}$	8.7	6.3	1.1	0.4
	HIRAX	-	-	SKA1 B2
z range	0.78-1.28	1.28-1.78	1.78-2.28	0.0-0.47
m^*	23.0	26.1	27.0	22.1
$\mathrm{SN_{tot}}$	28.5	9.4	3.8	5.8

Table 1. Optimised magnitude cutoffs, m^*, as well as cumulative signal to noise values for all experiments and redshift bins. Individual redshift bins of HIRAX are better than SKA1-MID also due to the higher number of ℓ bins that contribute.

count slope at the acceptable cost of increasing the (negligible) shot-noise at these redshifts. For high-redshift foreground bins, however, shot-noise increases and m^* needs to be higher to account for this.

Fig. 6 shows the optimised signal to noise as a function of multipole for all considered experiment and redshift combinations. Maps in each foreground redshift bin are correlated with one single redshift bin of LSST, separated from the foreground by $\Delta z = 0.1$ and ranging up to $z = 3.9$. Low redshift foreground bins benefit from a wider background sample containing a larger number of galaxies. Therefore, they often perform better than high redshift bins, especially in the case for HIRAX. The sensitivity of HIRAX is best at comparably small scales, where the power spectrum drops $\sim \ell^2$ (see e.g. Fig. 3). The shot noise, however, becomes the dominant error on smaller scales. The 512 dish design for HIRAX performs surprisingly well, as even in this case the interferometer noise remains subdominant.

Figure 7 shows the cumulative signal to noise which reaches levels of ~ 30 for individual redshift bins. The performance of SKA1-MID and HIRAX is similar for single ℓ bins, but HIRAX covers a larger multipole range. Both
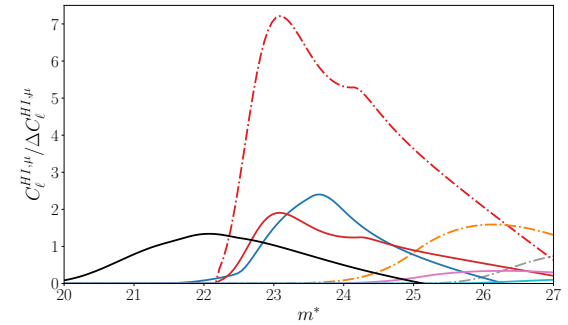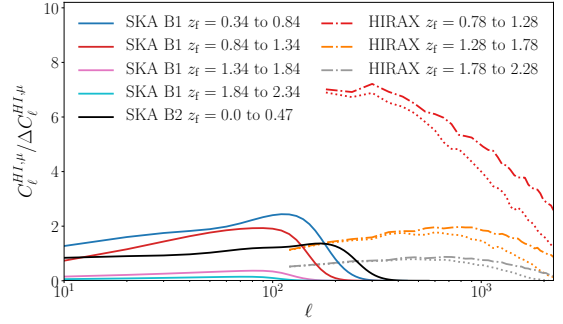

Figure 6. *Upper panel:* The expected signal to noise ratio of the magnification signal for the combinations HIRAX 1024 (dotted-dashed lines), HIRAX 512 (dotted lines) and SKA1 (solid lines) with LSST. We use different foreground redshift bins, always combined with one single non-overlapping background bin. Shot noise largely dominates, therefore the 512 dish version of HIRAX performs surprisingly well compared to the full array with 1024 dishes. *Lower panel:* The optimisation of the signal to noise ratio as a function of magnitude cutoff m^*. This panel is for single ℓ bins only, for SKA1-MID $\ell = 80$ and for HIRAX $\ell = 200$. These values were chosen to lie within the experiment's range of maximum sensitivity.
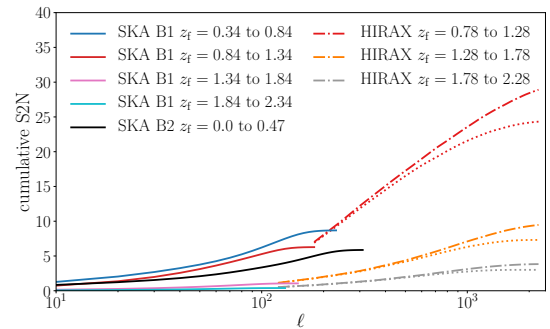

Figure 7. This plot shows the cumulative signal to noise ratio, Equation (22). For HIRAX especially, the error is dominated by the galaxy shot noise. Therefore even the down-scaled design with 512 dishes yields very similar results compared to the full proposal with 1024 dishes.

experiments yield best results at intermediate redshifts of $0.6 < z < 1.3$. As they are sensitive to different angular scales, most of their constraining power can be combined.

5 CONCLUSIONS

In this paper we proposed the use of HI intensity maps from large sky surveys with forthcoming radio arrays in cross-correlation with background optical galaxy samples from Stage IV photometric surveys, in order to detect the cosmic magnification signal.

We then derived predictions for the signal-to-noise ratio of the magnification signal from the foreground HI maps acting on background galaxies. We considered the survey combinations HIRAX with LSST and SKA1-MID with LSST. The signal-to-noise was optimised by changing the galaxy magnitude threshold m^* for LSST, since a lower magnitude cutoff boosts the magnification signal. Due to their different resolutions and mode operations, the information provided by the HIRAX interferometer is complimentary to the data gathered by SKA1-MID in autocorrelation (single dish) mode. A detection seems likely with forecasted cumulative signal to noise ratios in the range of ~ 30, but a more detailed analysis with appropriate simulations will be needed to fully assess all relevant sources of errors, e.g. foreground contamination residuals and cleaning effects. Foreground residuals are not expected to be significant in the cross-correlation between HI intensity maps and galaxies. The loss of long-wavelength radial modes in the HI data is also not expected to have a significant deteriorating effect on this observable. However, it would be useful to properly account and quantify both of these effects by extending the cross-correlation simulations studies performed in Witzemann et al. (2019); Cunnington et al. (2019a,b) – we leave this for future work. We also note that the choice of redshift binning could be reconsidered to make the analysis more realistic for a foreground cleaned HI survey. Furthermore, using realistic simulated LSST catalogues we can implement and test the performance of scale-dependent optimal weighting functions (Yang & Zhang 2011).

To conclude, our derived forecasts for the signal-to-noise for this detection suggest that it will certainly be possible once the data is available, and that it will be complementary to measurements using optical foreground samples with completely different systematics.

REFERENCES

Abate A., et al., 2012
Abbott T., et al., 2016, Mon. Not. Roy. Astron. Soc., 460, 1270

Alonso D., Bull P., Ferreira P. G., Maartens R., Santos M. G., 2015, The Astrophysical Journal, 814, 145
Amendola L., et al., 2018, Living Rev. Rel., 21, 2
Bacon D. J., Refregier A. R., Ellis R. S., 2000, Mon. Not. Roy. Astron. Soc., 318, 625
Bacon D. J., et al., 2018, Submitted to: Publ. Astron. Soc. Austral.
Bartelmann M., Schneider P., 2001, Phys. Rept., 340, 291
Battye R. A., Browne I. W. A., Dickinson C., Heron G., Maffei B., Pourtsidou A., 2013, Mon. Not. Roy. Astron. Soc., 434, 1239
Bernstein G., Jain B., 2004, ApJ, 600, 17
Bonvin C., Durrer R., 2011, Phys. Rev., D84, 063505
Bull P., Ferreira P. G., Patel P., Santos M. G., 2015, The Astrophysical Journal, 803, 21
Cunnington S., Wolz L., Pourtsidou A., Bacon D., 2019a
Cunnington S., Harrison I., Pourtsidou A., Bacon D., 2019b, Mon. Not. Roy. Astron. Soc., 482, 3341
Duncan C., Joachimi B., Heavens A., Heymans C., Hildebrandt H., 2014, Mon. Not. Roy. Astron. Soc., 437, 2471
Gabasch A., et al., 2006, A&A, 448, 101
Garcia-Fernandez M., et al., 2018, Mon. Not. Roy. Astron. Soc., 476, 1071
Hall A., Bonvin C., Challinor A., 2013, Phys. Rev. D, 87, 064026
Heymans C., et al., 2012, Mon. Not. Roy. Astron. Soc., 427, 146
Hildebrandt H., van Waerbeke L., Erben T., 2009, A&A, 507, 683
Hui L., Gaztañaga E., Loverde M., 2007, Phys. Rev. D, 76, 103502
Jain B., Taylor A., 2003, Phys. Rev. Lett., 91, 141302
Kaiser N., Wilson G., Luppino G. A., 2000
Kilbinger M., 2015, Rept. Prog. Phys., 78, 086901
LSST Science Collaboration et al., 2009, arXiv e-prints, p. arXiv:0912.0201
Lewis A., Challinor A., Lasenby A., 2000, ApJ, 538, 473
Limber D. N., 1954, ApJ, 119, 655
Loverde M., Afshordi N., 2008, Phys. Rev. D, 78, 123506
Mandelbaum R., 2018, Ann. Rev. Astron. Astrophys., 56, 393
Menard B., Bartelmann M., 2002, Astron. Astrophys., 386, 784
Menard B., Scranton R., Fukugita M., Richards G., 2010, Mon. Not. Roy. Astron. Soc., 405, 1025
Newburgh L. B., et al., 2016, in Ground-based and Airborne Telescopes VI. p. 99065X (arXiv:1607.02059), doi:10.1117/12.2234286
Santos M., et al., 2015, Advancing Astrophysics with the Square Kilometre Array (AASKA14), p. 19
Santos M. G., et al., 2017, preprint, (arXiv:1709.06099)
Schechter P., 1976, ApJ, 203, 297
Scranton R., et al., 2005, ApJ, 633, 589
Smith R. E., et al., 2003, Mon. Not. Roy. Astron. Soc., 341, 1311
Takahashi R., Sato M., Nishimichi T., Taruya A., Oguri M., 2012, Astrophys. J., 761, 152
Taylor A. N., Kitching T. D., Bacon D. J., Heavens A. F., 2007, MNRAS, 374, 1377
Van Waerbeke L., Hildebrandt H., Ford J., Milkeraitis M., 2010, Astrophys. J., 723, L13
Wittman D. M., Tyson J. A., Kirkman D., Dell'Antonio I., Bernstein G., 2000, Nature, 405, 143
Witzemann A., Alonso D., Fonseca J., Santos M. G., 2019, Mon. Not. Roy. Astron. Soc., 485, 5519
Yang X., Zhang P., 2011, Mon. Not. Roy. Astron. Soc., 415, L45
Zhang P., Pen U.-L., 2006, MNRAS, 367, 169
Ziour R., Hui L., 2008, Phys. Rev. D, 78, 123517
van Uitert E., et al., 2018, Mon. Not. Roy. Astron. Soc., 476, 4662
van Waerbeke L., et al., 2000, Astron. Astrophys., 358, 30